Published in final edited form as:
Ultrasound Med Biol. 2015 January ; 41(1): 222–234. doi:10.1016/j.ultrasmedbio.2014.07.001.

Ultrasound-based Measurement of Molecular Marker Concentration in Large Blood Vessels: A Feasibility Study

Shiying Wang,
Department of Biomedical Engineering, University of Virginia, Charlottesville, VA 22908, USA

F. William Mauldin Jr.,
Department of Biomedical Engineering, University of Virginia, Charlottesville, VA 22908, USA

Alexander L. Klibanov, and
Division of Cardiovascular Medicine and Department of Biomedical Engineering, University of Virginia, Charlottesville, VA 22908, USA

John A. Hossack
Department of Biomedical Engineering and Electrical and Computer Engineering, University of Virginia, Charlottesville, VA 22908, USA

Abstract

Ultrasound molecular imaging has demonstrated efficacy in pre-clinical studies for cancer and cardiovascular inflammation. However, these techniques often require lengthy protocols due to waiting periods or additional control microbubble injections. Moreover, they are not capable of quantifying molecular marker concentration in human tissue environments that exhibit variable attenuation and propagation path lengths. Our group recently investigated a modulated Acoustic Radiation Force (ARF)-based imaging sequence, which was demonstrated to detect targeted adhesion independent of control measurements. In the present study, this sequence was tested against various experimental parameters to determine feasibility for quantitative measurements of molecular marker concentration. Results demonstrated that measurements obtained from the sequence (residual-to-saturation ratio, R_{resid}) were independent of acoustic pressure and attenuation ($p > 0.13$, n = 10)when acoustic pressures were sufficiently low. The R_{resid} parameter exhibited a linear relationship with measured molecular marker concentration ($R^2 > 0.94$). Consequently, feasibility was demonstrated *in vitro*, for quantification of molecular marker concentration in large vessels using a modulated ARF-based sequence. Moreover, these measurements were independent of absolute acoustic reflection amplitude and used short imaging protocols(3 min) without control measurements.

(Corresponding author), Mail: 415 Lane Road, MR5 Building, Room 2121, Charlottesville, VA 22908, USA, Phone: (434) 243-5866; Fax: (434) 982-3870; jh7fj@virginia.edu.

Keywords

Ultrasound; molecular imaging; quantitative measurement; acoustic radiation force

Introduction

Microbubbles typically comprise of micrometer-sized low solubility gas core stabilized with a shell that acts as a diffusion barrier. Thanks to their high reflectivity of acoustic energy, microbubbles are the predominant ultrasound contrast agent. In addition to their use as a blood tracer, they can also be used for enhanced molecular imaging and drug/gene delivery (De Jong et al., 1992; Deshpande et al., 2010; Ferrara et al., 2007; Klibanov, 2002; Lindner, 2004; Mayer and Bekeredjian, 2008). In ultrasound-based targeted molecular imaging, ligands are matched to molecular markers associated with the disease of interest (e.g. ICAM-1 and P-selectin for cardiovascular disease) and are conjugated to the microbubble shell. Consequently, the specific ligand-receptor bond allows targeted microbubbles to adhere to specific regions of the vascular endothelium – providing an increased ultrasound echo signal indicating the presence of specific molecular markers on the vessel wall (Kornmann et al., 2010; Lindner et al., 2001; Villanueva et al., 1998; Weller et al., 2002). In order to increase adhesion of targeted microbubbles to the vessel wall, multiple ligands can be incorporated on the microbubble shell(Ferrante et al., 2009). Acoustic radiation force (ARF) is frequently applied to increase binding efficiency of microbubbles to potential sites, for example, in large vessel environments with high flow velocity and shear force (Dayton et al., 1999; Gessner et al., 2012; Rychak et al., 2007; Zhao et al., 2004). At present, ultrasound molecular imaging techniques are still mainly limited to pre-clinical applications.

The detection and isolation of echo signal derived from the molecularly bound microbubbles (adherent microbubbles) is essential in ultrasound-based targeted molecular imaging. Signals from surrounding tissue and freely circulating microbubbles must be suppressed to prevent false positive detection of adherent microbubbles. Typically, the combination of nonlinear signal detection (e.g. pulse inversion or harmonic imaging) and lengthy waiting periods (e.g. 15 – 30 min) is used to isolate signals from adherent microbubbles (Deshpande et al., 2010; Lindner et al., 2001; Phillips and Gardner, 2004; Phillips, 2001; Pochon et al., 2010). To decrease the procedure time, several “fast-imaging” methods (Hu et al., 2013; Pysz et al., 2012a, 2012b) and real-time imaging methods (Zhao et al., 2007; Gessner et al., 2010; Hu et al., 2010; Needles et al., 2009) have been developed for small vessel environments. Low-pass inter-frame filtering or pre- and post-burst subtraction are often used in these methods to separate signals of adherent microbubbles from free circulating microbubbles. In addition, with the assistance of ARF, recent studies have also demonstrated ultrasound targeted molecular imaging in large vessel environments using some new techniques(Mauldin et al., 2012; Patil et al., 2011; Wang et al., 2013b). In summary, state-of-the-art ultrasound molecular imaging methods have demonstrated efficacy in pre-clinical studies for detection and monitoring of various types of cancers (Bzyl et al., 2011; Fischer et al., 2010; Pysz et al., 2010)as well as cardiovascular inflammation (Kaufmann et al., 2007; Masseau et al., 2012). However, these approaches possess some limitations such as requiring a “control injection” (i.e. separate injection with non-targeted microbubbles) in

order to estimate the non-specific “background” signal. Consequently, the entire procedure times are still quite long (up to 30 – 40 min) due to injection of multiple microbubble populations and waiting periods needed between consecutive injections(Lindner et al., 2000; Masseau et al., 2012; Pysz et al., 2012b). This characteristic is undesirable because lengthy or complex imaging protocols could delay clinical adoption and also directly, or indirectly, increase procedure costs. Additionally, none of these methods have proven capable to quantify the molecular marker concentration in human tissue environments where attenuation and imaging path lengths are highly variable. The ability to achieve quantitative measurements of molecular marker concentration with non-invasive, low cost ultrasound holds value in a number of possible clinical applications. For example, quantitative measurements could facilitate time serial monitoring of disease or therapy at the molecular level or enable the establishment of measurement thresholds as a basis for treatment or interventions.

To meet the desired goals of quantitative molecular marker measurements with fast, simple imaging protocols, our group recently investigated a new modulated ARF-based imaging sequence. This strategy uses relatively short imaging protocols (3 min) that did not require lengthy waiting periods(Wang et al., 2013a). Briefly, this sequence provided constant ARF for a given period and collected acoustic data of adherent microbubbles continuously, both with application and after cessation of ARF. Parameters related to acoustic response of microbubbles were extracted and used to quantify the difference between specific and non-specific adhesion of microbubbles. Although quantitative assessment of disease progression has been demonstrated in small blood vessel environment(Bachawal et al., 2013; Pysz et al., 2012a, 2012b), these methods relied on absolute signal magnitude, which assumes consistent attenuation and path lengths to the disease site, which is highly variable in human imaging environments. Additionally, groups have used percent contrast coverage area as a quantitative measurement(Pysz et al., 2012a, 2012b). This approach attempts to quantify the percentage of pixels in the target region that contain adherent microbubbles. While demonstrated effective in cancers environments as a quantitative measurement proportional to microvessel density(Pysz et al., 2012a, 2012b), it does not allow for measurements of actual marker concentration. In this paper, we demonstrate that it is feasible to achieve quantitative measurements of molecular marker concentration in large vessel environments by using a modulated ARF-based imaging sequence. The effects of acoustic pressures, intensities, and attenuation on the modulated ARF-based imaging sequence are studied. The measured concentrations of molecular markers are correlated with parameter extracted from the imaging sequence.

Methods

In vitro experiment setup

Large blood vessel environments were mimicked using flow phantoms as described in previous studies (Fig. 1)(Hall et al., 1997; Wang et al., 2012). Briefly, the liquid channels were molded using borosilicate glass rods (McMaster-Carr, Robbinsville, NJ, USA) possessing a diameter of 4.0 mm, which were placed horizontally inside a custom designed phantom holder (Applied Rapid Technologies, Fredericksburg, VA, USA). The mixture of

gelatin (6.1%, w/w, Type B, Fisher Scientific, Pittsburgh, PA, USA), agar (2.2%, w/w, Acros Organics, Geel, Belgium) and graphite (1.8%, w/w, < 20 μm, Sigma-Aldrich, St. Louis, MO, USA) were dissolved in boiling water and then poured into the phantom holder with glass rods at a temperature of approximate 75 °C. The glass rods were slowly removed after the phantom was allowed to cool to room temperature. The thickness of the phantom was kept constant at approximately 8 mm from the top vessel wall to the phantom surface. All liquid channels were determined to possess a smooth, specular reflecting inner surface using both optical andacoustic assessments.

Microbubbles used in this study were synthesized biotinylated lipid shelled microbubbles (mean diameter ≈ 2.2 μm, standard deviation of diameter ≈ 1.5 μm, median diameter ≈ 1.9 μm) (Klibanov, 2002; Klibanov et al., 1999). Empirically, it is preferable to use ultrasound pulses for pushing these microbubbles at a transmit frequency of approximate 4 MHz(Patil et al., 2011). Microbubbles were diluted in 0.9% Sodium Chloride Irrigation, USP (Baxter Healthcare, Deerfield, IL, USA) at a concentration of 0.5×10^6/mL. The concentration of microbubbles in this aqueous solution was measured and maintained by a Coulter counter (Coulter Multisizer 3, Beckman Coulter, Brea, CA, USA). Fresh microbubble dispersion was prepared every 10 min during the experiments. In addition, 0.5% (w/w) bovine serum albumin (BSA, Sigma-Aldrich, St. Louis, MO, USA) solution was added into the microbubble solution to further prevent non-specific adhesion (Hernot et al., 2012; Wang et al., 2013c).

Two types of phantom channels were used in the study: targeted phantom channels and control phantom channels. Targeted phantom channels were created by incubation with streptavidin (AnaSpec, Fremont, CA, USA) solution (concentration ranging from 1 to 50 μg/mL)for 12 h (4 °C)followed by another incubation with 10% (w/w) BSA solution for 10 min (4 °C). Control phantom channels were created by incubation with 10% (w/w) BSA solution alone for 12 h (4 °C). Each phantom channel was used for one trial only in order to avoid effects from residual microbubbles(Wang et al., 2013c).

Experiments were performed by injecting microbubble solution through phantom channels at a given flow velocity (6 – 10 cm/s) using a programmable syringe pump (PHD ULTRA, Harvard Apparatus, Holliston, MA, USA) for 180 s. The proposed phantom channel diameter and flow velocities were similar to the typical diameter and average flow velocities in large human vessels, such as in the brachial artery(4 mm and 9 cm/s)(Ku, 1997; Levenson et al., 2000; Safar et al., 1981).

Modulated acoustic radiation force (ARF)-based imaging sequence

Similar to a previous study by our group (Wang et al., 2013a), the modulated ARF-based imaging sequence continuously collected acoustic echo data for 180 s at a frame rate of 4 Hz (Fig. 2). The sequence was divided into three sections: 10 s of imaging alone (0 – 10 s), 70 s of imaging and ARF (10 – 80 s), and 100 s of imaging alone (80 – 180 s). The imaging pulses were single cycle plane wave pulses at a center frequency of 4.5 MHz. Echo data obtained from three consecutive imaging pulses were used to form one image frame using conventional dynamic receive focusing. All imaging pulses for the entire 180 s sequence were identical, and were neither amplitude nor phase modulated. The peak negative pressure

(PNP) of imaging pulses in this study ranged from 17.3 to 91.6 kPa, measured using a calibrated Onda GL-0200 hydrophone (Onda, Sunnyvale, CA, USA), with corresponding mechanical indices (MI) ranging from 0.008 to 0.043. In addition, the ARF pulses were 15-cycle plane wave pulses at a center frequency of 4.5 MHz. The average pulse repetition frequency (PRF) of ARF pulses ranged from 5 to 15 kHz. And the PNP of ARF pulses ranged from 46.5 to 189.5 kPa, with corresponding MI ranging from 0.022 to 0.089. It was confirmed by fluorescent microscopy in previous studies that adherent microbubbles would accumulate along the bottom liquid channels with application of ARF pulses (Mauldin et al., 2012; Patil et al., 2011). The above imaging sequence was programmed on a Verasonics programmable ultrasound scanner (Verasonics, Redmond, WA, USA) equipped with an ATL L12-5 38 mm linear array transducer (Philips Healthcare, Andover, MA, USA).

For each trial, 720 consecutive image frames were processed using MATLAB (Mathworks, Natick, MA, USA). For each image frame, the average signal magnitude (M) was calculated within the region of interest (ROI) (Wang et al., 2013a), which was located in the center of the bottom channel wall and possessed a depth of 0.2 mm and a width of 2 mm. The depth location of the ROI was determined automatically by detecting the location of maximum average signal magnitude. The ROI also spanned 10 consecutive laterally adjacent A-lines to decrease the effects of non-uniform distribution of adherent microbubbles along the bottom channel wall. The signal magnitude curve ($M(t)$, $0 < t < 180$ s) was obtained by computing M for all 720 image frames.

It has been demonstrated in a previous study (Wang et al., 2013a) that $M(t)$ for targeted phantom channels expresses an exponential increase approaching a saturation magnitude during the second section of the imaging sequence with application of ARF (10 – 80 s); and an exponential decay approaching a residual magnitude during the third section of the imaging sequence after cessation of ARF (80 – 180 s). The ratio of residual to saturation signals (R_{resid}) was used to separate targeted adhesion from non-specific adhesion.

$$R_{\text{resid}} = \left(\frac{M_{\text{resid}} - M_{\text{init}}}{M_{\text{satu}} - M_{\text{init}}} \right) \times 100$$

M_{init} and M_{resid} were the initial signal magnitude (signal magnitude at $t = 5$ s) and residual signal magnitude (signal magnitude at $t = 180$ s), respectively (Fig. 2). M_{satu} was the saturated signal magnitude(signal magnitude at $t = 80$ s for targeted channels). In this study, R_{resid} was calculated and used to compare targeted adhesion levels in different experimental conditions. According to the models described in a previous study by our group (Wang et al., 2013a), M_{satu} represented the full saturation of adherent microbubbles (both specific and non-specific) and M_{init} represented the background signal magnitude of the wall in absence of adherent microbubbles. After cessation of ARF, only targeted ligand-receptor bound microbubbles remained and the remaining adherent microbubble concentration is quantified by M_{resid}. The R_{resid} parameter combines the signal magnitude-dependent parameters (M_{init}, M_{satu}, and M_{resid}) to produce a measure that is independent of absolute signal magnitude. It represents the percentage of wall containing targeted ligand-receptor bound microbubbles. Consequently, in this study we hypothesize that R_{resid} has a linear relationship with

molecular marker concentration along the vessel wall and that R_{resid} is independent of attenuation or path length effects on acoustic signal magnitude.

Measurements of molecular marker concentration

In order to estimate the concentration of streptavidin bound to the phantom channels at different incubation concentrations (1 – 50 μg/mL), Eu^{3+}-labelled streptavidin (DELFIA Eu-N1 Streptavidin, PerkinElmer, Waltham, MA, USA) was used to incubate phantom channels at corresponding incubation concentrations (1 – 50 μg/mL) using exactly the same procedure as for regular streptavidin – 12 h incubation followed by another incubation with 10% (w/w) BSA solution for 10 min. One centimeter long phantom channels were harvested and then the inner channel surfaces were washed for 15 s using 100 μL Enhancement Solution (DELFIA, PerkinElmer, Waltham, MA, USA). The enhancement solution was then collected; and the corresponding Eu^{3+}-fluorescence was measured in a dissociation-enhanced time-resolved spectrofluorometry (SPECTRAmax GEMINI-XS, Molecular Devices, Sunnyvale, CA, USA). Finally, the concentration of Eu^{3+}-labelled streptavidin in the samples was computed by comparing with the fluorescence signal of a reference solution. The measurements were repeated 5 times for each incubation concentration of Eu^{3+}-labelled streptavidin(Suonpää et al., 1992).

Experiment design

The first set of experiments was designed to test the effects of acoustic pressures of both imaging and ARF pulses on the parameter R_{resid}. The acoustic parameters (PNP and MI) of different groups (from G_{P1} to G_{P9}) are listed in Table 1. For all 9 groups, the following parameters remained the same: flow velocity (6 cm/s), incubation concentration of streptavidin (50 μg/mL), and PRF of ARF pulses (5 kHz). For each group, 10 trials of targeted phantom channels and 10 trials of control phantom channels were performed in different phantoms to eliminate measurement bias from phantom-to-phantom or batch-to-batch microbubble variations. The R_{resid} parameter of each group was calculated and compared. For Student's *t*-tests, differences were considered statistically significant only if the calculated *p*-value was less than 0.05. Based on the results, the group with best performance (details described below in results) was selected as the "reference group"and the acoustic parameters of the reference group were used for the next set of experiments.

The next set of experiments was designed to test the effect of attenuation, and thus absolute signal magnitude, on the parameter R_{resid}. The flow and acoustic parameters of the aforementioned reference group were implemented. One layer of 0.8 mm-thick rubber membrane(Neoprene Rubber, McMaster-Carr, Robbinsville, NJ, USA) was placed between the transducer and phantom for the first group, G_{A1}. For the second group, G_{A2}, two layers of the same rubber membrane were placed between the transducer and phantom. The measured acoustic parameters of PNP and MI of the two groups are listed in Table 2. Based on the measurements, one and two layers of 0.8 mm-thick rubber membrane provided 2.1 dB and 4.4 dB attenuation relative to the reference group (G_{P5}), respectively. For each group, 10 trials of targeted phantom channels and 10 trials of control phantom channels were performed.

The third set of experiments was designed to test the effect of ARF pulse intensities (time-averaged intensity of ARF pulses) on the parameter R_{resid}. Our previous study demonstrated the effect of lower PRF of ARF pulses (0.5 and 2.5 kHz)(Wang et al., 2013a). In this study, two groups (G_{PRF1} and G_{PRF2}) of experiments with higher PRF of ARF pulses (10 and 15 kHz) were performed. Except for ARF pulse intensity, other flow and acoustic parameters used in this part of experiments were the same as the aforementioned reference group. For each group, 10 trials of targeted phantom channels and 10 trials of control phantom channels were tested.

The fourth set of experiments was designed to test the ability of this technique to quantitatively measure molecular marker concentration based on the parameter R_{resid}. The flow and acoustic parameters of different groups of experiments (G_{V1C1} to G_{V2C6}) are listed in Table 2. For the first 6 groups (G_{V1C1}, G_{V1C2}, G_{V1C3}, G_{V1C4}, G_{V1C5}, G_{V1C6}), the flow velocity remained the same at 6 cm/s and incubation concentration of streptavidin increased from 1 to 50 μg/mL. For the second 6 groups (G_{V2C1}, G_{V2C2}, G_{V2C3}, G_{V2C4}, G_{V2C5}, G_{V2C6}), flow velocity remained the same at a higher level, 10 cm/s. All other flow and acoustic parameters used in these 12 groups of experiments, except for flow velocity and incubation concentration of streptavidin, were kept the same as the aforementioned reference group. For each group, 10 trials of targeted phantom channels and 10 trials of control phantom channels were tested.

Results

Effect of varying acoustic pressures of imaging and ARF pulses on R_{resid}

The signal magnitude curves of both targeted and control phantom channels for different acoustic conditions listed in Table 1(G_{P1} to G_{P9}) are illustrated in Fig. 3. Each curve represents the average over 10 trials. The signal magnitude curves of both targeted and control phantom channels for all 9 groups increased with application of ARF (10 – 80 s). After cessation of ARF (80 – 180 s), signal magnitude returned to the baseline level for control phantom channels; and maintained a significantly higher residual level for targeted phantom channels ($p < 0.001$, n = 10). The R_{resid} parameter for both targeted and control phantom channels across various acoustic conditions listed in Table 1 are shown in Fig. 4. The mean R_{resid} values were below 5% for control phantom channels at different groups; and were above 25% for targeted phantom channels at different groups. In addition, for each group, the R_{resid} of targeted phantom channels was significantly higher than that of the control phantom channels ($p < 0.001$, n = 10).

At any given imaging pulse acoustic pressure (17.3, 46.1, or 91.6 kPa), the median acoustic pressure (106.0 kPa) of ARF pulses tested in the study resulted in both the highest saturation and residual average signal magnitude for targeted phantom channels. In addition, the highest acoustic pressure (189.5 kPa) of ARF pulses resulted in the lowest residual signal magnitudes of targeted phantom channels. Similarly, the three groups (G_{P3}, G_{P6}, and G_{P9}) with application of the highest ARF pulse pressure expressed a relatively lower R_{resid} value of approximate 30%. There was no significant difference between any two of these three groups ($p > 0.40$, n = 10). In addition, other groups (G_{P1}, G_{P2}, G_{P4}, G_{P5}, G_{P7}, and G_{P8})

expressed a relatively higher R_{resid} value of approximate 60%, with no significant difference between any two of the 6 groups (p>0.13, n = 10).

At a given ARF pulse pressure (46.5, 106.0, or 189.5 kPa), higher imaging pulse pressure resulted in higher signal magnitude for both targeted and control phantom channels. However, the shape of the average signal magnitude curves (both targeted and control phantom channels) remained similar for all three imaging pulse pressures (17.3, 46.1, 91.6 kPa). With regards to the R_{resid} parameter in targeted phantom channels, at a given ARF pulse pressure, there was no significant difference in R_{resid} values between any two of the three groups at different imaging pulse pressure (p>0.16 for PNP_{ARF} of 46.5 kPa, p>0.80 for PNP_{ARF} of 106.0 kPa, and p>0.40 for PNP_{ARF} of 189.5 kPa, n = 10).

Based on the results in Fig. 3 and Fig. 4, the group of G_{P5} was selected as the reference group for the following reasons: (1) the G_{P5}group was among the groupings with highest R_{resid} (~ 60%); (2) the voltage profile applied for both imaging and ARF pulses were the same (3 V) which meant that there were no possible error derived from switching of the power supply between high voltage and low voltage profiles. The acoustic and flow parameters of the reference group were used for the following sets of experiments.

Effects of attenuation on R_{resid}

The signal magnitude curves of both targeted and control phantom channels for different acoustic conditions listed in Table 2 (G_{A1} and G_{A2}) are illustrated in Fig. 5. Each curve represents the average over 10 trials. Compared to the reference group (G_{P5}) results depicted in Fig. 3e,a higher attenuation resulted in lower signal magnitude for both targeted and control phantom channels. However, the shape of average signal magnitude curves for both targeted and control phantom channels remained similar at different attenuation levels. The R_{resid} parameters of targeted phantom channels were significantly higher than those of control phantom channels (p < 0.001, n = 10). In addition, there was no significant difference (p > 0.28, n = 10) in R_{resid} values between any two of the three groups (G_{A1}, G_{A2}, and G_{P5}).

Effects of ARF intensity on R_{resid}

The signal magnitude curves of both targeted and control phantom channels for different time-averaged ARF intensities (G_{PRF1} and G_{PRF2}) are illustrated in Fig. 6. Each curve represented the average over 10 trials. Compared to the reference group (G_{P5}) in Fig. 3, higher ARF intensities resulted in higher signal magnitude levels for only the targeted phantom channels. For control phantom channels, both the saturation signal magnitude (t = 80 s) and the shape of signal magnitude curve remained similar for the three groups (G_{PRF1}, G_{PRF2}, and G_{P5}). The R_{resid} parameters in targeted phantom channels were significantly higher than those of control phantom channels (p < 0.001, n = 10). In addition, R_{resid} values in the G_{PRF2}group were significantly lower than that of the reference group (p < 0.05, n = 10).

Correlation between R_{resid} and streptavidin concentration under different flow velocities

Six representative signal magnitude curves from targeted phantom channels with different incubation concentrations of streptavidin and flow velocities, listed in Table 3(G_{V1C1}, G_{V1C4}, G_{V1C6}, G_{V2C1}, G_{V2C4}, and GV2C6), are illustrated in Fig. 7. Each curve represents the average over 10 trials. For each of the two flow velocities (6 and 10 cm/s), higher incubation concentration resulted in higher residual levels. For the two groups with incubation concentration of 1 μg/mL (G_{V1C1} and G_{V2C1}), the residual signal magnitudes were not significantly higher than the corresponding initial signal magnitudes (p>0.16, n = 10). In other groups with the same incubation concentrations but different flow velocity, the higher flow velocity resulted in lower residual levels.

The measured molecular marker (Eu^{3+} -labelled streptavidin)surface concentration($C_{Molecule}$) through spectrofluorometry linearly increased(R^2 = 0.985) with incubation concentration ($C_{Incubation}$) (Fig. 8a). There were 5 trials for each of the incubation concentrations. The linear relationship between molecular marker concentration and incubation concentration can be described as:

$$C_{\mathrm{Molecule}}=(6.9\pm1.0)\times10^{-2}C_{\mathrm{Incubation}}$$

The unit of $C_{Molecule}$ and $C_{Incubation}$ are 10^3 /μm^2 and μg/mL, respectively. The residual signal magnitude (M_{resid}) was demonstrated to be linear with molecular marker concentration at different flow velocities (R^2 = 0.985 for 6 cm/s, R^2 = 0.983 for 10 cm/s) (Fig. 8b and 8d). Additionally, the R_{resid} parameter was also demonstrated to be linear with molecular marker concentration at different flow velocities (R^2 = 0.998 for 6 cm/s, R^2 = 0.949 for 10 cm/s) (Fig. 8c and 8e).

In order to further characterize the performance of R_{resid} as a quantitative measure of molecular marker concentration, the detection sensitivity was calculated as the minimum difference in molecular marker concentration that could provide significantly different R_{resid} values. The detection sensitivity was not the same at different molecular marker concentrations – lower molecular marker concentrations were associated with higher detection sensitivity for both flow velocities (6 and 10 cm/s). At the 6 cm/s flow velocity, the highest and lowest detection sensitivities were 0.9×10^3 /μm^2 and 1.3×10^3/μm^2, respectively (Fig. 8c). At the flow velocity of 10 cm/s, the highest and low detection sensitivities were 2.2×10^3/μm^2 and 2.6×10^3/μm^2, respectively (Fig. 8e).

Discussion

A summary of tested hypotheses, results, and conclusions from this study are summarized in Fig. 9. As illustrated in Fig. 3 and Fig. 4, groups (G_{P3}, G_{P6}, and G_{P9}) with the highest ARF acoustic pressure (189.5 kPa) resulted in the lowest residual signal magnitudes in targeted phantom channels and relatively lower R_{resid} (~ 30%) values compared to the other six groups (listed in Table 1). Additionally, targeted channels in the other six groups (G_{P1}, G_{P2}, G_{P4},G_{P5}, G_{P7}, and G_{P8}) with varied imaging and ARF acoustic pressures exhibited the same relatively high R_{resid} values (~ 60%). Consequently, below a certain limit in ARF acoustic

pressure (between 106.0 and 189.5 kPa in this study), the results demonstrated that parameter R_{resid} of targeted channels was independent of both imaging and ARF acoustic pressures. Although a low MI of 0.089 was maintained, which was below the limit at which microbubble rupture is common (Bouakaz et al., 2005), it is hypothesized that the relatively high ARF acoustic pressure (189.5 kPa) destroyed or dislodged adherent microbubbles thus resulting in lower residual signal magnitudes as well as lower R_{resid} values. In addition, as shown in Fig. 5, all targeted channels under varied levels of attenuation (G_{P5}, G_{A1}, and G_{A2}) exhibited the same R_{resid} values (~ 60%), which further demonstrates that the R_{resid} parameter is independent of absolute signal magnitude. Consequently, these results demonstrate that when operating below certain acoustic pressure limits, the R_{resid} parameter is a measurement that is independent of acoustic pressure and tissue attenuation.

In similar experiments performed with varied levels of time averaged ARF intensity, instead of peak intensity, it was observed that the higher time averaged intensity resulted in lower R_{resid} values. Compared to group G_{P5} (Fig. 3e), the targeted signal magnitude curveat highest time averaged intensity exhibited a sudden magnitude drop immediately after cessation of ARF (t = 80 s), which is illustrated by arrows and labels as the difference between magnitude levels M_1 and M_2 in Fig. 10a and 10b. It is hypothesized that the additional signal magnitude and rapid magnitude drop is due to layering of microbubbles that occurs with increased ARF. This accumulation of microbubbles can result in two groups: (1) a lower sub-layer of microbubbles which directly interacts with the streptavidin coated channel wall; (2) an upper sub-layer of microbubbles which accumulates on top of the lower sub-layer due to higher ARF intensity but is not accessible to the streptavidin along the channel wall. Therefore, immediately after cessation of ARF the upper sub-layer of microbubbles were rapidly freed from the aggregation because there was no molecular binding force to retain them. In contrast, the microbubbles in the lower sub-layer, which are able to interact with the streptavidin, underwent the normal exponential decay to a steady-state residual level. The rapid dissipation of the former group of microbubbles is therefore hypothesized to have resulted in the sudden magnitude drops uniquely demonstrated by groups G_{PRF1} and G_{PRF2}. Consequently, M_1 and M_2 represent the signal magnitudes of the sum of two sub-layers and the lower sub-layer alone, respectively (Fig. 10a and 10b). If the microbubble layering effect was taken into account by replacing M_1 with M_2 while calculating R_{resid} values using Eqn. 1, there was actually no significant difference of R_{resid} values (~ 60%) between any two of the three groups (G_{P5}, G_{PRF1}, and G_{PRF2}) with a minimum p value of 0.57 (n = 10). Hence, results suggested that parameter R_{resid} was again a robust measurement, which was immune to ARF intensity if the microbubble layering effect is taken into account. Note that in these R_{resid} measurements, it was assumed that the upper sub-layer of microbubbles was completely dissipated within 1 s (from t = 80 s to 81 s).

The results in Fig. 8a demonstrate excellent linearity between molecular marker concentration and incubation concentration (Eqn. 2, R^2= 0.985). Previous studies demonstrated that ICAM-1 expression levels for endothelial cells can be as high as approximately 5×10^6 per cell (Almenar-Queralt et al., 1995; Dustin and Springer, 1988). The endothelial cell surface area was approximately 10^3 μm^2(Adamson, 1993). Hence the

site densities of ICAM-1 ranged approximately from less than 50(unstimulated) to 5×10^3 (stimulated)sites/μm^2(Almenar-Queralt et al., 1995; Dustin and Springer, 1988). The experimental results corresponded well with our measured streptavidin concentrations (approximately 0 to $4.0\times10^3 \mu m^{-2}$). However, it is anticipated that the measured molecular marker concentration of Eu^{3+}-labelled streptavidin through spectrofluorometry was overestimated in this study. The average pore size in agarose gelatin phantom was approximately 200 nm (Bauman et al., 2004; Griess et al., 1993). Presumably, Eu^{3+}-labelled streptavidin molecules could permeate the phantom through the holes on surface during incubation. As a result, when washing the phantom channels, enhancement solution would take away Eu^{3+} from not only the streptavidin molecules attached onto the channel surface, but also a portion of streptavidin molecules embedded inside the phantom within a certain depth. This portion of streptavidin molecules embedded inside the phantom actually could not participate in the binding process with targeted microbubbles.

The linear regression analysis on the R_{resid} values versus streptavidin concentration illustrated in Fig. 8 demonstrated the feasibility of parameter R_{resid} as a quantitative measurement of molecular marker concentration. However, the detection sensitivity decreased with higher flow rates due to less residual microbubbles, which was caused by higher shear forces. Based on the site densities of ICAM-1 (approximately 50 to 5×10^3 sites/μm^2) (Almenar-Queralt et al., 1995; Dustin and Springer, 1988), the detection sensitivities at flow rates of both 6 and 10 cm/s would be sufficient to distinguish blood vessels with stimulated versus unstimulated endothelial cells.

Conclusion

In summary, feasibility was demonstrated in this study for quantification of molecular marker concentration using a new modulated ARF-based imaging sequence and extraction of the residual-to-saturation ratio(R_{resid}) parameter. Various experimental parameters including acoustic pressures, intensities and attenuation were used to test this imaging strategy. This technique exhibited many desirable characteristics: (1) the quantitative measurement parameter(R_{resid}) is proportional to molecular marker concentration, and within certain bounds, is independent of attenuation and absolute signal magnitude; (2)no separate control groups were required; (3) short imaging protocols were used with scan time of3 min and no extra waiting period. However, the quantitative measurement was demonstrated to be dependent on flow rates, with lower detection sensitivity at higher flow rates. Overall, this study demonstrates feasibility of quantitative molecular marker measurements using non-invasive ultrasound-based targeted molecular imaging. It represents a promising technique with high potential for improved ultrasound molecular imaging for real-time detection and quantification of early disease markers for atherosclerosis in large arteries *in vivo*.

Acknowledgments

This work was supported by NIH R01 EB001826 and R01 HL111077. The content is solely the responsibility of the authors and does not necessarily represent the official views of the NIH. The authors would like to thank Elizabeth B. Herbstand Claudia Y. Wang for their help with the experiments; Sunil Unnikrishnan for his advice on microbubbles and molecular marker concentrations; and Verasonics, Inc. for its technical support.

References

Adamson RH. Microvascular endothelial cell shape and size in situ. Microvasc. Res. 1993; 46:77–88. [PubMed: 8412854]

Almenar-Queralt A, Duperray A, Miles LA, Felez J, Altieri DC. Apical topography and modulation of ICAM-1 expression on activated endothelium. Am. J. Pathol. 1995; 147:1278–1288. [PubMed: 7485391]

Bachawal SV, Jensen KC, Lutz AM, Gambhir SS, Tranquart F, Tian L, Willmann JK. Earlier detection of breast cancer with ultrasound molecular imaging in a transgenic mouse model. Cancer Res. 2013; 73:1689–1698. [PubMed: 23328585]

Bauman MA, Gillies GT, Raghavan R, Brady ML, Pedain C. Physical characterization of neurocatheter performance in a brain phantom gelatin with nanoscale porosity: steady-state and oscillatory flows. Nanotechnology. 2004; 15:92–97.

Bouakaz A, Versluis M, De Jong N. High-speed optical observations of contrast agent destruction. Ultrasound Med. Biol. 2005; 31:391–399. [PubMed: 15749563]

Bzyl J, Lederle W, Rix A, Grouls C, Tardy I, Pochon S, Siepmann M, Penzkofer T, Schneider M, Kiessling F, Palmowski M. Molecular and functional ultrasound imaging in differently aggressive breast cancer xenografts using two novel ultrasound contrast agents (BR55 and BR38). Eur. Radiol. 2011; 21:1988–1995. [PubMed: 21562807]

Dayton P, Klibanov A, Brandenburger G, Ferrara K. Acoustic radiation force in vivo: a mechanism to assist targeting of microbubbles. Ultrasound Med. Biol. Biol. 1999; 25:1195–1201.

De Jong N, Hoff L, Skotland T, Bom N. Absorption and scatter of encapsulated gas filled microspheres: theoretical considerations and some measurements. Ultrasonics. 1992; 30:95–103. [PubMed: 1557838]

Deshpande N, Needles A, Willmann JK. Molecular ultrasound imaging: current status and future directions. Clin. Radiol. 2010; 65:567–581. [PubMed: 20541656]

Dustin M, Springer T. antigen-1 (LFA-1) interaction with intercellular adhesion molecule-1 (ICAM-1) is one of at least three mechanisms for lymphocyte adhesion to cultured endothelial cells. J. Cell Biol. 1988; 107:321–331. [PubMed: 3134364]

Ferrante EA, Pickard JE, Rychak J, Klibanov A, Ley K. Dual targeting improves microbubble contrast agent adhesion to VCAM-1 and P-selectin under flow. J. Control. Release. 2009; 140:100–107. [PubMed: 19666063]

Ferrara K, Pollard R, Borden M. Ultrasound microbubble contrast agents: fundamentals and application to gene and drug delivery. Annu. Rev. Biomed. Eng. 2007; 9:415–447. [PubMed: 17651012]

Fischer T, Thomas A, Tardy I, Schneider M, Hünigen H, Custodis P, Beyersdorff D, Plendl J, Schnorr J, Diekmann F, Gemeinhardt O. Vascular endothelial growth factor receptor 2-specific microbubbles for molecular ultrasound detection of prostate cancer in a rat model. Invest. Radiol. 2010; 45:675–684. [PubMed: 20733504]

Gessner R, Lukacs M, Lee M, Cherin E, Foster FS, Dayton PA. High-resolution, high-contrast ultrasound imaging using a prototype dual-frequency transducer: in vitro and in vivo studies. IEEE Trans. Ultrason. Ferroelectr. Freq. Control. 2010; 57:1772–1781. [PubMed: 20679006]

Gessner RC, Streeter JE, Kothadia R, Feingold S, Dayton PA. An in vivo validation of the application of acoustic radiation force to enhance the diagnostic utility of molecular imaging using 3-D ultrasound. Ultrasound Med. Biol. Biol. 2012; 38:651–660.

Griess GA, Guiseley KB, Serwer P. The relationship of agarose gel structure to the sieving of spheres during agarose gel electrophoresis. Biophys. J. 1993; 65:138–148. [PubMed: 8369423]

Hall TJ, Bilgen M, Insana MF, Krouskop TA. Phantom materials for elastography. IEEE Trans. Ultrason. Ferroelectr. Freq. Control. 1997; 44:1355–1365.

Hernot S, Unnikrishnan S, Du Z, Shevchenko T, Cosyns B, Broisat A, Toczek J, Caveliers V, Muyldermans S, Lahoutte T, Klibanov AL, Devoogdt N. Nanobody-coupled microbubbles as novel molecular tracer. J. Control. Release. 2012; 158:346–353. [PubMed: 22197777]

Hu X, Caskey CF, Mahakian LM, Kruse DE, Beegle JR, Declèves A-E, Rychak JJ, Sutcliffe PL, Sharma K, Ferrara KW. In vivo validation and 3D visualization of broadband ultrasound molecular imaging. Am. J. Nucl. Med. Mol. Imaging. 2013; 3:336–349. [PubMed: 23901359]

Hu X, Zheng H, Kruse DE, Sutcliffe P, Stephens DN, Ferrara KW. A sensitive TLRH targeted imaging technique for ultrasonic molecular imaging. IEEE Trans. Ultrason. Ferroelectr. Freq. Control. 2010; 57:305–316. [PubMed: 20178897]

Kaufmann BBA, Sanders JMJ, Davis C, Xie A, Aldred P, Sarembock IJ, Lindner JR. Molecular imaging of inflammation in atherosclerosis with targeted ultrasound detection of vascular cell adhesion molecule-1. Circulation. 2007; 116:276–284. [PubMed: 17592078]

Klibanov A. Ultrasound contrast agents: development of the field and current status. Contrast Agents II. 2002; 222:73–106.

Klibanov AL, Hughes MS, Villanueva FS, Jankowski RJ, Wagner WR, Wojdyla JK, Wible JH, Brandenburger GH. Targeting and ultrasound imaging of microbubble-based contrast agents. Magma Magn. Reson. Mater. Physics, Biol. Med. 1999; 8:177–184.

Kornmann LM, Reesink KD, Reneman RS, Hoeks APG. Critical appraisal of targeted ultrasound contrast agents for molecular imaging in large arteries. Ultrasound Med. Biol. 2010; 36:181–191. [PubMed: 20018434]

Ku DN. Blood Flow in Arteries. Annu. Rev. Fluid Mech. 1997; 29:399–434.

Levenson JA, Peronneau PA, Simon A, Safar ME. Pulsed Doppler: determination of diameter, blood flow velocity, and volumic flow of brachial artery in man. Cardiovasc. Res. 2000; 45:23–26. [PubMed: 10728308]

Lindner JR. Microbubbles in medical imaging: current applications and future directions. Nat. Rev. Drug Discov. 2004; 3:527–532. [PubMed: 15173842]

Lindner JR, Song J, Christiansen J, Klibanov AL, Xu F, Ley K. Ultrasound assessment of inflammation and renal tissue injury with microbubbles targeted to P-selectin. Circulation. 2001; 104:2107–2112. [PubMed: 11673354]

Lindner JR, Song J, Xu F, Klibanov AL, Singbartl K, Ley K, Kaul S. Noninvasive Ultrasound Imaging of Inflammation Using Microbubbles Targeted to Activated Leukocytes. Circulation. 2000; 102:2745–2750. [PubMed: 11094042]

Masseau I, Davis MJ, Bowles DK. Carotid inflammation is unaltered by exercise in hypercholesterolemic Swine. Med. Sci. Sports Exerc. 2012; 44:2277–2289. [PubMed: 22776877]

Mauldin FWJ, Dhanaliwala AH, Patil AV, Hossack JA. Real-time targeted molecular imaging using singular value spectra properties to isolate the adherent microbubble signal. Phys. Med. Biol. 2012; 57:5275–5293. [PubMed: 22853933]

Mayer CR, Bekeredjian R. Ultrasonic gene and drug delivery to the cardiovascular system. Adv. Drug Deliv. Rev. 2008; 60:1177–1192. [PubMed: 18474407]

Needles A, Couture O, Foster FS. A method for differentiating targeted microbubbles in real time using subharmonic micro-ultrasound and interframe filtering. Ultrasound Med. Biol. 2009; 35:1564–1573. [PubMed: 19632763]

Patil AV, Rychak JJ, Klibanov AL, Hossack JA. Real-time technique for improving molecular imaging and guiding drug delivery in large blood vessels: in vitro and ex vivo results. Mol. Imaging. 2011; 10:238–247. [PubMed: 21521555]

Phillips P. Contrast pulse sequences (CPS): imaging nonlinear microbubbles. IEEE Ultrason. Symp. 2001:1739–1745.

Phillips P, Gardner E. Contrast-agent detection and quantification. Eur. Radiol. 2004; 14(Suppl 8):P4–P10. [PubMed: 15700327]

Pochon S, Tardy I, Bussat P, Bettinger T, Brochot J, Von Wronski M, Passantino L, Schneider M. BR55: a lipopeptide-based VEGFR2-targeted ultrasound contrast agent for molecular imaging of angiogenesis. Invest. Radiol. 2010; 45:89–95. [PubMed: 20027118]

Pysz MA, Foygel K, Rosenberg J, Gambhir SS, Schneider M, Willmann JK. Antiangiogenic cancer therapy: monitoring with molecular US and a clinically translatable contrast agent (BR55). Radiology. 2010; 256:519–527. [PubMed: 20515975]

Pysz MA, Guracar I, Foygel K, Tian L, Willmann JK. Quantitative assessment of tumor angiogenesis using real-time motion-compensated contrast-enhanced ultrasound imaging. Angiogenesis. 2012a; 15:433–442. [PubMed: 22535383]

Pysz MA, Guracar I, Tian L, Willmann JK. Fast microbubble dwell-time based ultrasonic molecular imaging approach for quantification and monitoring of angiogenesis in cancer. Quant. Imaging Med. Surg. 2012b; 2:68–80. [PubMed: 22943043]

Rychak JJ, Klibanov AL, Ley KF, Hossack JA. Enhanced targeting of ultrasound contrast agents using acoustic radiation force. Ultrasound Med. Biol. 2007; 33:1132–1139. [PubMed: 17445966]

Safar ME, Peronneau PA, Levenson JA, Toto-Moukouo JA, Simon AC. Pulsed Doppler: diameter, blood flow velocity and volumic flow of the brachial artery in sustained essential hypertension. Circulation. 1981; 63:393–400. [PubMed: 7449061]

Suonpää M, Markela E, Ståhlberg T, Hemmilä I. Europium-labelled streptavidin as a highly sensitive universal label. Indirect time-resolved immunofluorometry of FSH and TSH. J. Immunol. Methods. 1992; 149:247–253. [PubMed: 1593136]

Villanueva FS, Jankowski RJ, Klibanov S, Pina ML, Alber SM, Watkins SC, Brandenburger GH, Wagner WR. Microbubbles targeted to intercellular adhesion molecule-1 bind to activated coronary artery endothelial cells. Circulation. 1998; 98:1–5. [PubMed: 9665051]

Wang S, Hossack JA, Klibanov AL, Mauldin FW. Binding dynamics of targeted microbubbles in response to modulated acoustic radiation force. Phys. Med. Biol. 2013a; 59:465–484. [PubMed: 24374866]

Wang S, Mauldin FW, Hossack JA. Decorrelation-based adherent microbubble identification as a faster alternative to singular spectrum-based targeted molecular (SiSTM) imaging of large blood vessels. IEEE Ultrason. Symp. 2013b:1829–1832.

Wang S, Mauldin FWJ, Hossack JA. The physical source of adherent microbubble signal separation in singular spectrum-based targeted molecular imaging (SiSTM) of large vessels. IEEE Ultrason. Symp. 2012:2153–2156.

Wang S, Mauldin FWJ, Klibanov AL, Hossack JA. Modulating targeted adhesion of an ultrasound contrast agent to dysfunctional endothelium. Ann. Biomed. Eng. 2013c; 12:396–408.

Weller GER, Villanueva FS, Klibanov AL, Wagner WR. Modulating targeted adhesion of an ultrasound contrast agent to dysfunctional endothelium. Ann. Biomed. Eng. 2002; 30:1012–1019. [PubMed: 12449762]

Zhao S, Borden M, Bloch SH, Kruse DE, Ferrara KW, Dayton PA. Radiation-force assisted targeting facilitates ultrasonic molecular imaging. Mol. imaging Off. J. Soc. Mol. Imaging. 2004; 3:135–148.

Zhao S, Kruse DE, Ferrara KW, Dayton PA. Selective imaging of adherent targeted ultrasound contrast agents. Phys. Med. Biol. 2007; 52:2055–2072. [PubMed: 17404455]

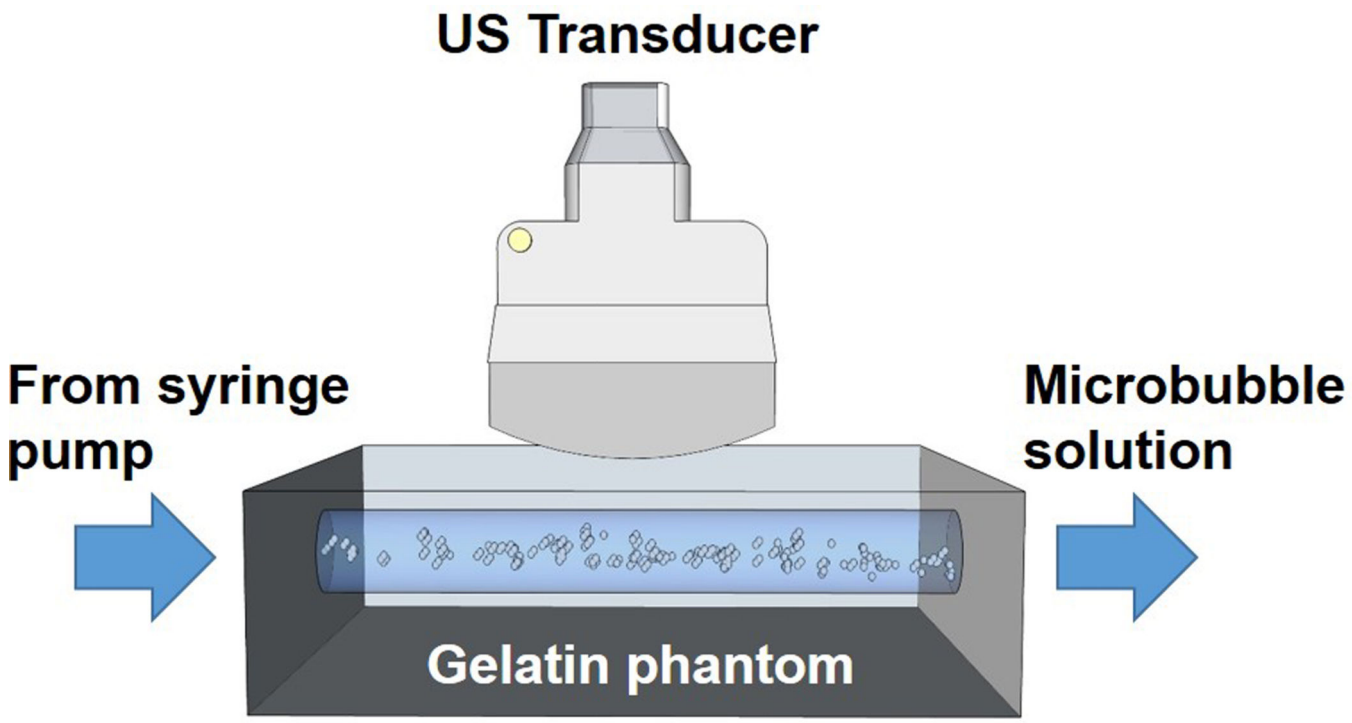

Figure 1.
The *in vitro* flow phantom setup. US: ultrasound.

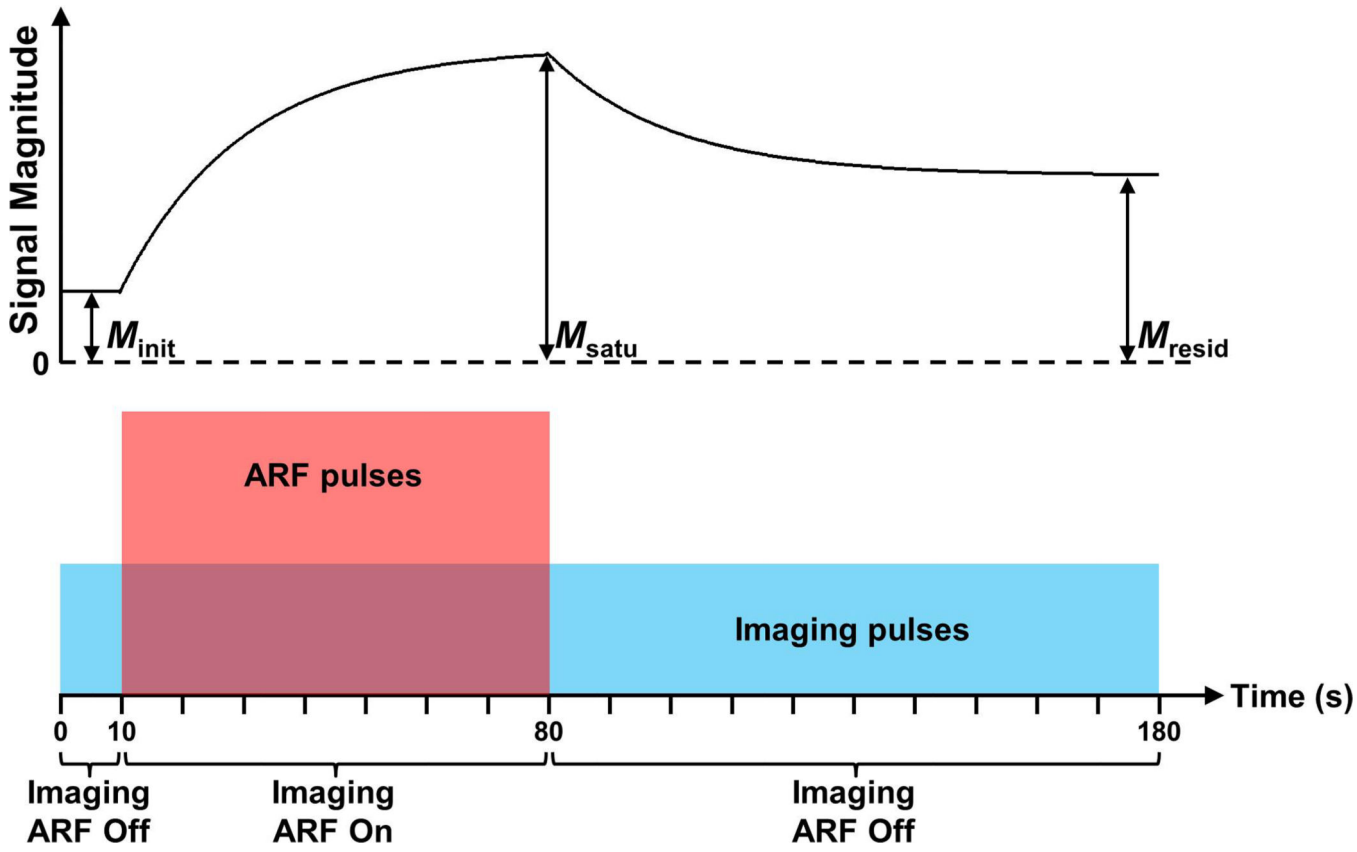

Figure 2.

Diagram of the modulated ARF-based imaging sequence (bottom) and corresponding representative signal magnitude curve (top). The signal magnitude curve is acquired in a region of interest corresponding to the lower vessel wall where radiation force leads to the aggregation of adherent microbubbles. Imaging and ARF pulses are represented with blue and red colors, respectively. The amplitudes of imaging and ARF pulses are not to scale.

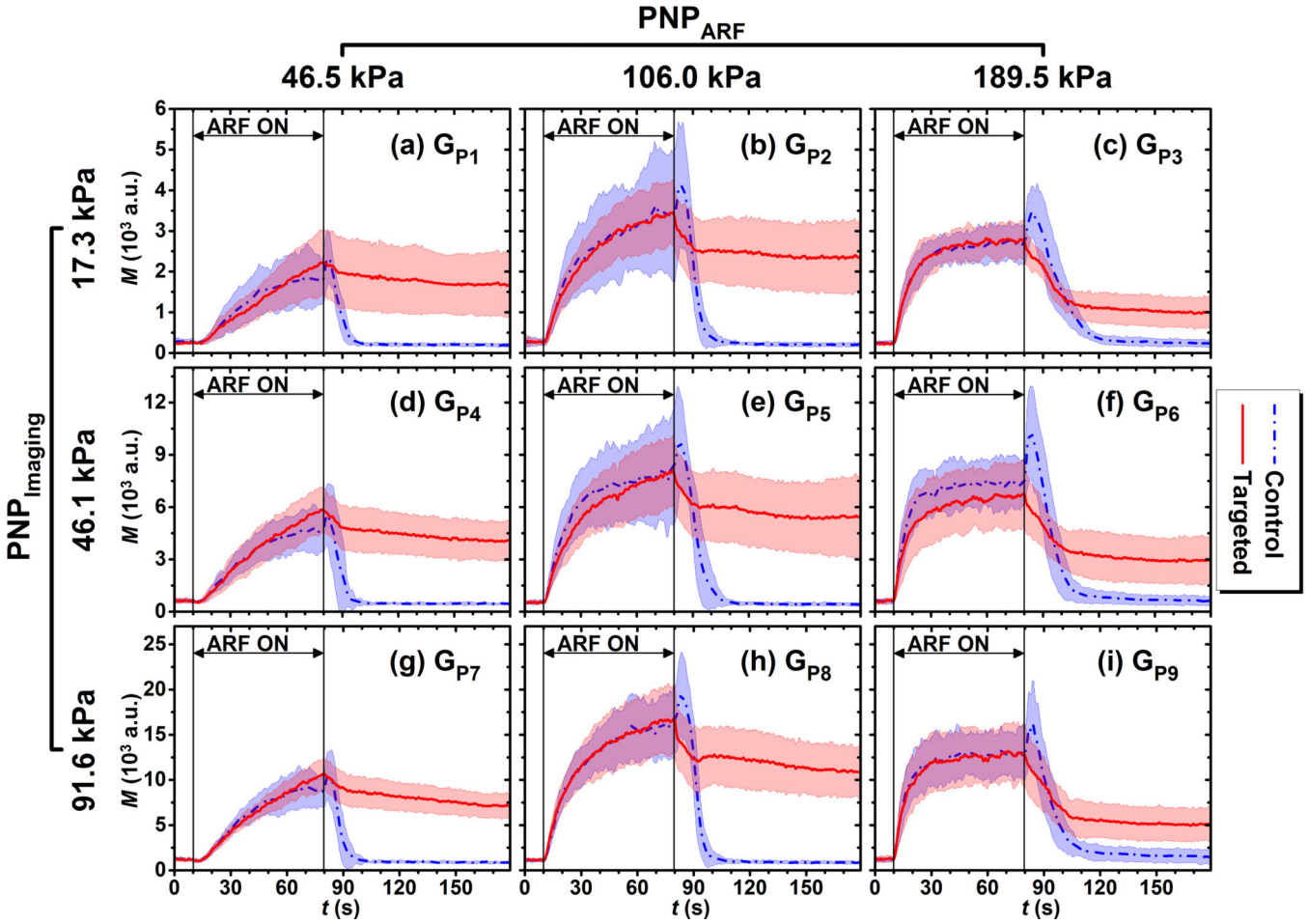

Figure 3.

Signal magnitude curves in regions of adherent microbubbles in control (blue) and targeted (red) phantom channels at different acoustic conditions listed in Table 1. (a) G_{P1}, (b) G_{P2}, (c) G_{P3}, (d) G_{P4}, (e) G_{P5}, (f) G_{P6}, (g) G_{P7}, (h) G_{P8}, (i) G_{P9}. Blue dash-dot and red solid lines indicate the mean values from 10 trials. Light color shadows indicate the corresponding error bars at the range of [mean ± standard deviation]. Different y-axis scales used to make comparison between curve shapes easier.

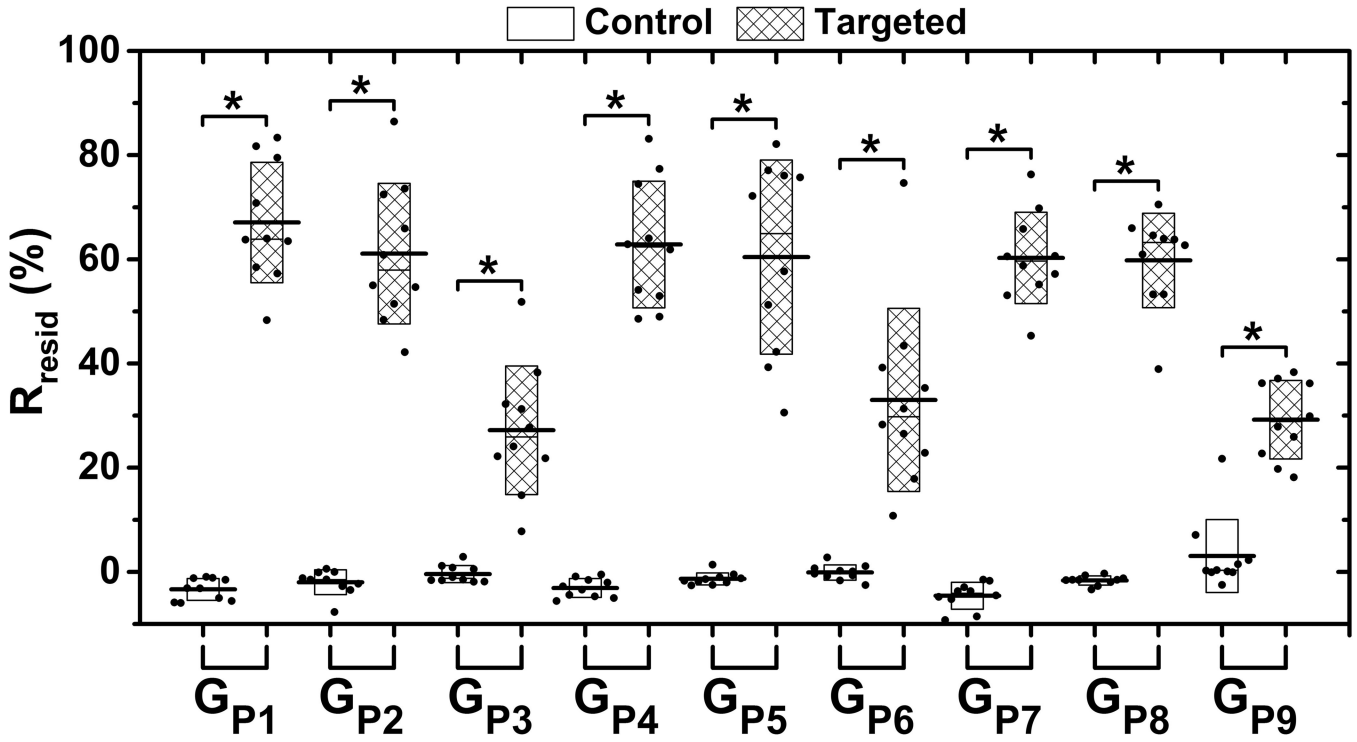

Figure 4.

The R_{resid} parameter across the different acoustic conditions listed in Table 1. Boxes (empty for control and filled for targeted phantom channels) show the range of [mean ± standard deviation]. Black lines located at the center of the boxes show the corresponding mean value from 10 trials. Raw data from 10 trials are shown as solid dots overlaid with corresponding boxes. For Student's *t*-test, *: $p < 0.001$, n = 10.

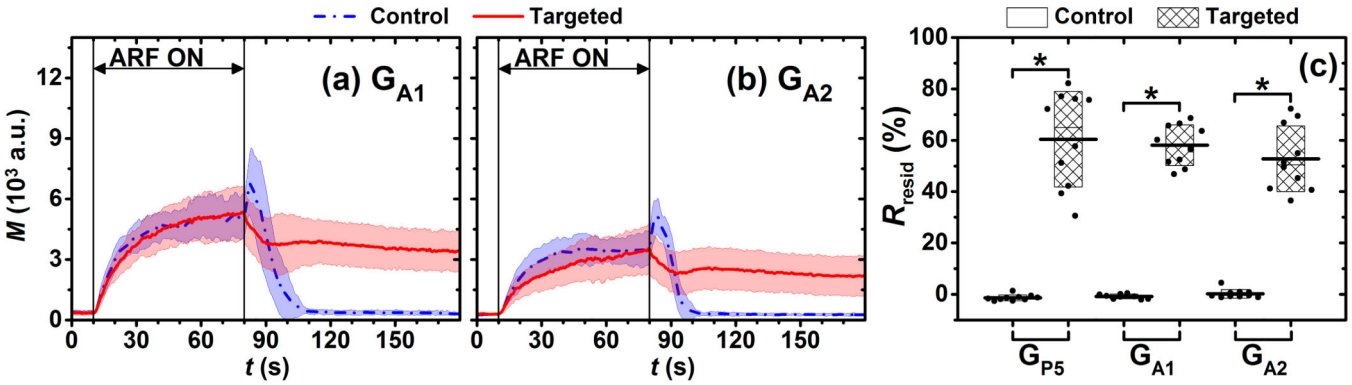

Figure 5.

Signal magnitude curves of adherent microbubbles in control (blue) and targeted (red) phantom channels at different attenuations listed in Table 2, (a) G_{A1}, the attenuation group with one rubber membrane layer (2.1 dB attenuation) and (b) G_{A2}, the attenuation group with two rubber membrane layers (4.4 dB attenuation). Blue dash-dot and red solid lines indicate the mean values from 10 trials. Light color shadows indicate the corresponding error bars at the range of [mean ± standard deviation]. (c) The R_{resid} parameter for G_{P5} (reference group), G_{A1}, and G_{A2}. Boxes (empty for control and filled for targeted phantom channels) show the range of [mean ± standard deviation]. Black lines located at the center of the boxes show the corresponding mean value from 10 trials. Raw data from 10 trials are depicted as solid dots overlaid with corresponding boxes. For Student's *t*-test, *: $p < 0.001$, n = 10.

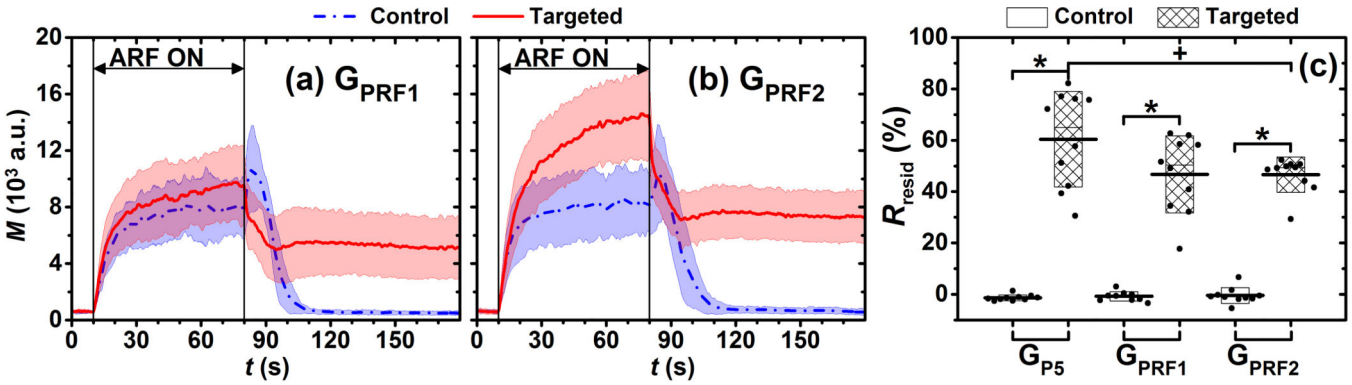

Figure 6.

Signal magnitude curves of adherent microbubbles in control (blue) and targeted (red) phantom channels at different PRF of ARF pulses, (a) G_{PRF1} and (b) G_{PRF2}. Blue dash-dot and red solid lines indicate the mean values from 10 trials. Light color shadows indicate the corresponding error bars at the range of [mean ± standard deviation]. (c) The R_{resid} parameter for groups of G_{P5} (reference group), G_{PRF1}, and G_{PRF2}. Boxes (empty for control and filled for targeted phantom channels) show the range of [mean ± standard deviation]. Black lines located at the center of the boxes show the corresponding mean value from 10 trials. Raw data from 10 trials are shown as solid dots overlaid with corresponding boxes. For Student's *t*-test, $^{+}p < 0.05$, *: $p < 0.001$, n = 10.

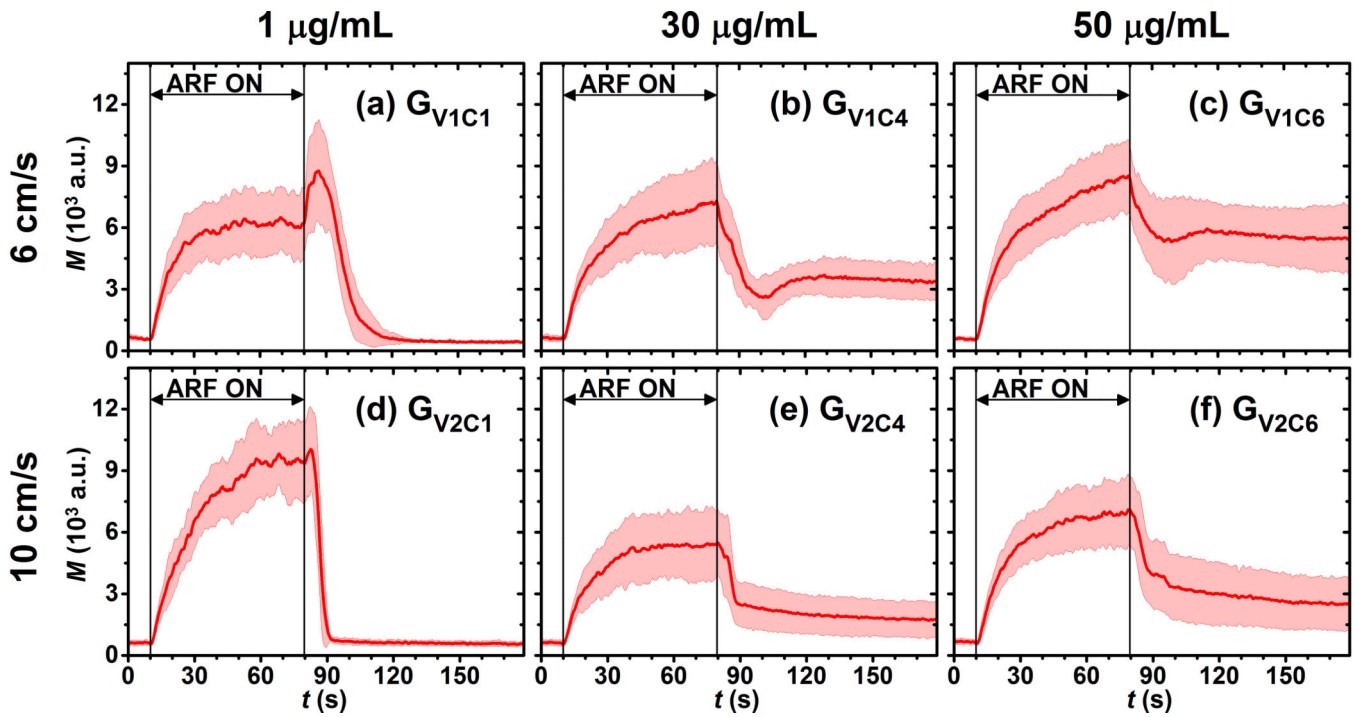

Figure 7.

Signal magnitude curves of adherent microbubbles in targeted phantom channels at different flow and incubation conditions listed in Table 3. (a) G_{V1C1}, (b) G_{V1C4}, (c) G_{V1C6}, (d) G_{V2C1}, (e) G_{V2C4}, (f) G_{V2C6}. Red solid lines indicate the mean values from 10 trials. Light color shadows indicate the corresponding error bars at the range of [mean ± standard deviation].

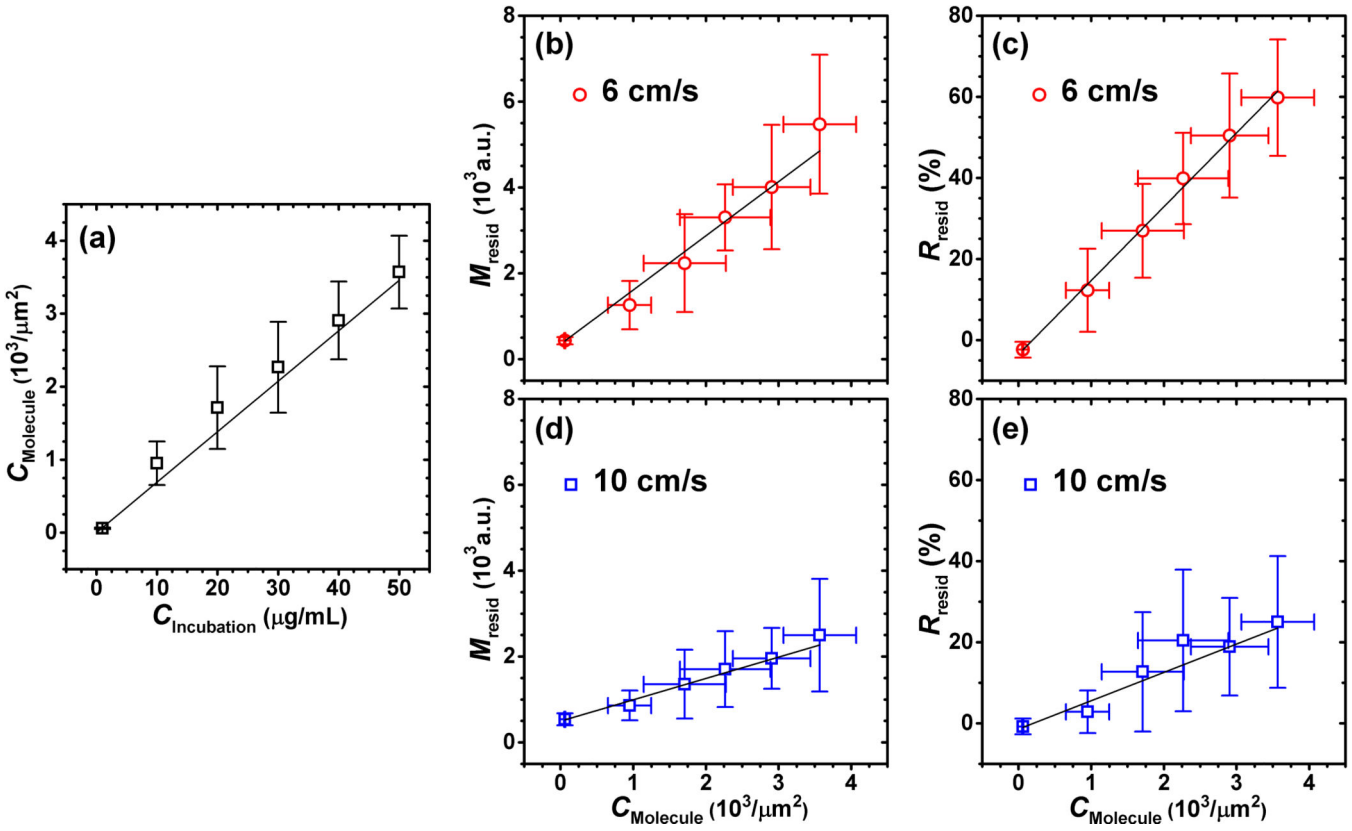

Figure 8.

(a) Relationship between incubation concentration ($C_{Incubation}$) and measured molecular marker concentration ($C_{Molecule}$) of Eu^{3+}-labelled streptavidin ($R^2 = 0.985$). Relationships between residual signal magnitude (M_{resid}) and molecular marker concentration at flow velocities of 6 cm/s ($R^2 = 0.985$) (b), and 10 cm/s ($R^2 = 0.983$) (d). Relationships between R_{resid} parameter and molecular marker concentration at flow velocities of 6 cm/s ($R^2 = 0.998$) (c), and 10 cm/s ($R^2 = 0.949$) (e). Black lines show the weighted linear fits; error bars show the range of [mean ± standard deviation].

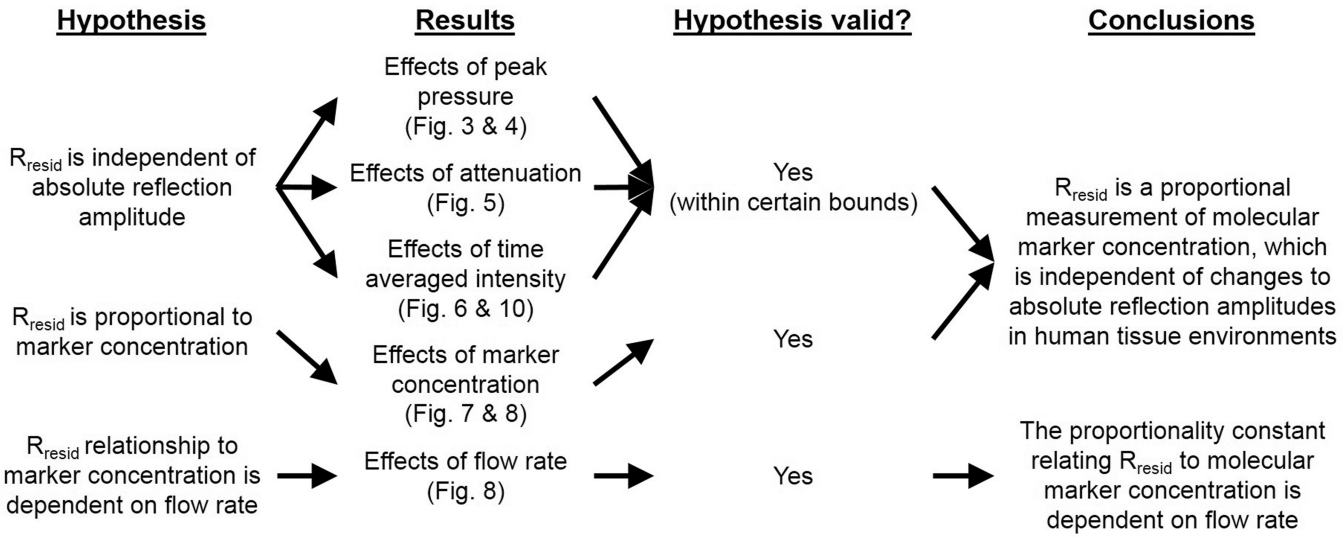

Figure 9.
Summary of tested hypotheses, results, and conclusions.

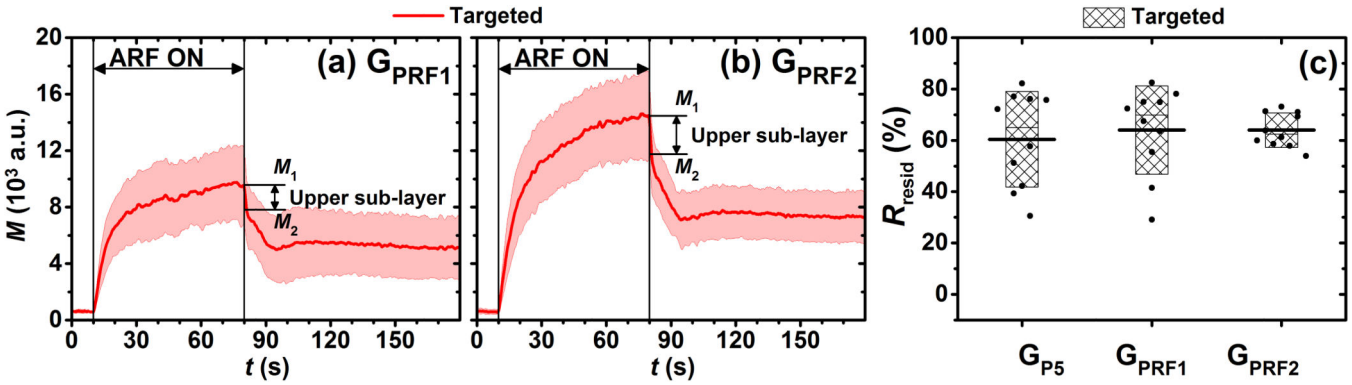

Figure 10.

Signal magnitude curves of adherent microbubbles in targeted phantom channels at different PRF of ARF pulses, (a) G_{PRF1} and (b) G_{PRF2}. Solid lines indicate the mean values from 10 trials. Light color shadows indicate the corresponding error bars at the range of [mean ± standard deviation]. M_1 is the maximum signal magnitude at t = 80 s. M_2 is the signal magnitude at t = 81 s. The signal magnitude of upper sub-layer of microbubbles is assumed to be $M_2 - M_1$. (c) The R_{resid} parameter for groups of G_{P5} (reference group), G_{PRF1}, and G_{PRF2}. Filled boxes show the range of [mean ± standard deviation]. Black lines located at the center of the boxes show the corresponding mean value from 10 trials. Raw data from 10 trials are shown as solid dots overlaid with corresponding boxes.

Table 1

Parameters of experiments to test effects of acoustic pressures

Parameter	Group name								
	G_{P1}	G_{P2}	G_{P3}	G_{P4}	G_{P5}	G_{P6}	G_{P7}	G_{P8}	G_{P9}
$PNP_{imaging}$ [a] (kPa)	17.3	17.3	17.3	46.1	46.1	46.1	91.6	91.6	91.6
$MI_{imaging}$ [b]	0.008	0.008	0.008	0.022	0.022	0.022	0.043	0.043	0.043
PNP_{ARF} [c] (kPa)	46.5	106.0	189.5	46.5	106.0	189.5	46.5	106.0	189.5
MI_{ARF} [d]	0.022	0.050	0.089	0.022	0.050	0.089	0.022	0.050	0.089

[a] Peak negative pressure of imaging pulses;

[b] Mechanical index of imaging pulses;

[c] Peak negative pressure of ARF pulses;

[d] Mechanical index of ARF pulses

Table 2

Parameters of experiments to test effects of attenuation

Parameter	Group name	
	G_{A1}[a]	G_{A2}[b]
$PNP_{imaging}$ (kPa)	28.9	25.3
$MI_{imaging}$	0.014	0.013
PNP_{ARF} (kPa)	83.1	63.6
MI_{ARF}	0.041	0.031

[a] The attenuation group with 2.1 dB attenuation

[b] The attenuation group with 4.4 dB attenuation

Table 3

Parameters of experiments for measurements of molecular marker concentration

Parameter	**Group name**					
	G_{V1C1}	**G_{V1C2}**	**G_{V1C3}**	**G_{V1C4}**	**G_{V1C5}**	**G_{V1C6}**
v^a (cm/s)	6	6	6	6	6	6
$C_{Incubation}$ ^{b} (μg/mL)	1	10	20	30	40	50
Parameter	Group name					
	G_{V2C1}	G_{V2C2}	G_{V2C3}	G_{V2C4}	G_{V2C5}	G_{V2C6}
v (cm/s)	10	10	10	10	10	10
$C_{Incubation}$ (μg/mL)	1	10	20	30	40	50

^{a}Flow velocity;

^{b}Incubation concentration of streptavidin